HHS Public Access

Author manuscript

Neuroimage. Author manuscript; available in PMC 2018 May 15.

Published in final edited form as:

Neuroimage. 2017 May 15; 152: 348–359. doi:10.1016/j.neuroimage.2017.02.029.

Reduction of across-run variability of temporal SNR in accelerated EPI time-series data through FLEET-based robust autocalibration

Anna I. Blazejewska[1,*], **Himanshu Bhat**[2], **Lawrence L. Wald**[1,3], and **Jonathan R. Polimeni**[1,3]

[1]Athinoula A. Martinos Center for Biomedical Imaging, Department of Radiology, Harvard Medical School, Massachusetts General Hospital, Charlestown, MA, USA

[2]Siemens Medical Solutions USA Inc., Charlestown, MA, USA

[3]Harvard-MIT Division of Health Sciences and Technology, Massachusetts Institute of Technology, Cambridge, MA, USA

Abstract

Temporal signal-to-noise ratio (tSNR) is a key metric for assessing the ability to detect brain activation in fMRI data. A recent study has shown substantial variation of tSNR between multiple runs of accelerated EPI acquisitions reconstructed with the GRAPPA method using protocols commonly used for fMRI experiments. Across-run changes in the location of high-tSNR regions could lead to misinterpretation of the observed brain activation patterns, reduced sensitivity of the fMRI studies, and biased results. We compared conventional EPI autocalibration (ACS) methods with the recently-introduced FLEET ACS method, measuring their tSNR variability, as well as spatial overlap and displacement of high-tSNR clusters across runs in datasets acquired from human subjects at 7T and 3T. FLEET ACS reconstructed data had higher tSNR levels, as previously reported, as well as better temporal consistency and larger overlap of the high-tSNR clusters across runs compared with reconstructions using conventional multi-shot (ms) EPI ACS data. tSNR variability across two different runs of the same protocol using ms-EPI ACS data was about two times larger than for the protocol using FLEET ACS for acceleration factors (R) 2 and 3, and one and half times larger for R=4. The level of across-run tSNR consistency for data reconstructed with FLEET ACS was similar to within-run tSNR consistency. The displacement of high-tSNR clusters across two runs (inter-cluster distance) decreased from ~8 mm in the time-series reconstructed using conventional ms-EPI ACS data to ~4 mm for images reconstructed using FLEET ACS. However, the performance gap between conventional ms-EPI ACS and FLEET ACS narrowed with increasing parallel imaging acceleration factor. Overall, the FLEET ACS method provides a simple solution to the problem of varying tSNR across runs, and therefore helps ensure that an assumption of fMRI analysis—that tSNR is largely consistent across runs—is met for accelerated acquisitions.

[*]Corresponding author: Athinoula A. Martinos Center for Biomedical Imaging, Massachusetts General Hospital, 149 Thirteenth St. Suite 2301, Charlestown, MA, 02129, USA. tel: +1617 7263-197; fax: +1 617 726-7422. ABLAZEJEWSKA@mgh.harvard.edu.

Graphical abstract

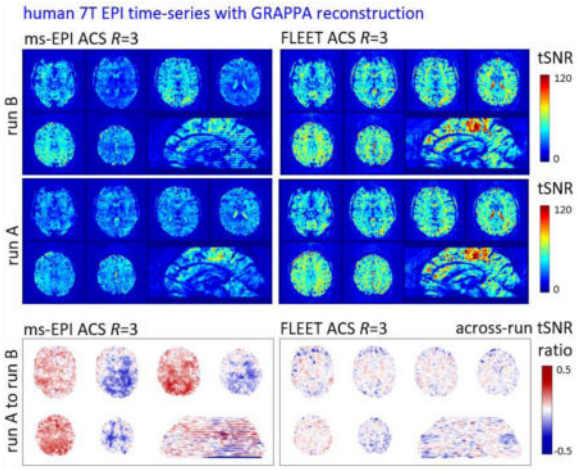

Keywords

FLEET; GRAPPA; temporal SNR; high-resolution fMRI; EPI autocalibration signal; respiratory artifacts; UHF fMRI; 7 Tesla MRI

Introduction

Temporal signal-to-noise ratio (tSNR) provides a crucial metric for assessing ability of an fMRI acquisition to detect subtle neuronally-driven changes in the measured time-series data. The detectability of a signal fluctuation of interest can be characterized by the functional contrast-to-noise ratio (fCNR), which is a joint function of both the tSNR and the percent signal change of the fluctuation of interest: fCNR = tSNR •S/S (Krüger et al., 2001; Wald, 2012; Wald and Polimeni, 2015). While the percent signal change (ΔS/S) induced by local brain activation in fMRI measurements using the blood oxygenation level-dependent (BOLD) contrast depends only on the efficacy of the stimulation and the neurovascular coupling and on the TE value (since $\Delta S/S = 1 - \exp(TE\ \Delta R_2^*)$), the tSNR provides a convenient metric that characterizes the detection power of the fMRI measurement in a way that is independent of the specifics of the stimulation, neuronal activation, and local physiology. Therefore, tSNR is a practically useful metric that can be employed when optimizing the sensitivity of the functional acquisition. There are several sources of noise captured by the tSNR metric that may affect fMRI signal. Physiological noise (e.g., respiratory changes and cardiac pulsation), instrumental noise (thermal noise and low frequency drifts due to the scanner or hardware instabilities), as well as noise originating from spontaneous neuronal activity have different relative influence on the fMRI signal fluctuations (Bianciardi et al., 2009). Because tSNR is also a function of the static image signal-to-noise ratio (SNR_0), it is affected by acquisition parameters such as the receive coil, flip angle, TE and voxel size. The relative contribution of thermal and physiological noise depending on these parameters has been investigated in different tissues and at different magnetic field strengths and receive coil combinations (Bodurka et al., 2007; Triantafyllou et al., 2016, 2011, 2005).

Single-shot echo-planar imaging (EPI) has become the imaging technique of choice for functional, diffusion, and perfusion MRI due to its ability to quickly and repeatedly image the entire brain. Parallel imaging (PI) techniques (Griswold et al., 2002; Pruessmann et al., 1999; Sodickson and Manning, 1997) allow decreased echo spacing and readout time in EPI acquisitions, therefore reducing geometric distortion artifacts, signal losses and T_2^* blurring (de Zwart et al., 2006; Griswold et al., 1999). Since the severity of these artifacts increases with the magnetic field strength, PI acceleration methods are especially beneficial for high-field fMRI leading to improved data quality and higher spatial resolution (de Zwart et al., 2002; Setsompop et al., 2016). The two most commonly used PI methods, sensitivity encoding (SENSE) (Pruessmann et al., 1999) and generalized autocalibrating partially parallel acquisitions (GRAPPA) (Griswold et al., 2002), undersample the k-space data during the acquisition by skipping encoding steps, thereby shortening the total readout time, then estimate the fully-sampled dataset using a small amount of calibration data. For anatomical imaging techniques (such as MPRAGE) the PI reconstruction can be "autocalibrated" by acquiring a small amount of fully-sampled autocalibration signal (ACS) data during the acquisition (consisting of a set of additional k-space lines) which can be used to estimate coil sensitivities or derive GRAPPA kernel weights to reconstruct the undersampled data. However, for accelerated fMRI acquisitions where the under-sampled image data measurement is repeated many times during the time series, a fully sampled pre-scan can be acquired once per time-series to serve as calibration data, with the assumption that the calibration data remains valid throughout the time series and thus changes related to subject motion over time are negligible.

Functional imaging studies often consist of multiple runs of the same fMRI protocol performed with varying paradigms (such as different tasks) or the same paradigm repeated multiple times to increase sensitivity of the measurements. In conventional fMRI analysis it is typically implicitly assumed that the tSNR is largely consistent across runs, and therefore runs are often either simply concatenated or contrasted using straightforward fixed-effects analyses. However, recent work has shown that tSNR may indeed vary dramatically between multiple runs of accelerated single-shot EPI acquisitions reconstructed with the GRAPPA method, which is commonly used for fMRI acquisitions (Cheng, 2012). Large differences in the spatial distribution of tSNR values across multiple runs, such as varying location of the high-tSNR regions where the detection sensitivity is the highest, will cause false positives and negatives (if an activation is located in a high-tSNR region in one run and in a low-tSNR region in the next one) leading to misinterpretation of the brain activation patterns therefore reducing the accuracy of fMRI studies.

For accelerated EPI reconstructions, ACS data for GRAPPA kernel calibration are conventionally acquired as multi-shot segmented EPI (ms-EPI), with the number of segments equal to the acceleration factor (R) of the data acquisition. This is conventionally done on a consecutive-slice manner which allows for longitudinal magnetization recovery before proceeding to the next segment. Namely the first interleave is acquired for all the slices before acquiring the second interleave. Thus, any two interleaves are acquired a time TR apart, which can lead to artifacts related to the subject's breathing and head motion during the TR period. Since the ACS data are used to calculate the GRAPPA kernel applied to the time-series images, errors introduced by motion or breathing may result in lower

tSNR in a subset of the slices. In conventional slice-interleaved acquisitions (where slices are acquired first stepping through the odd-numbered slices and then the even), this ACS data artifact is propagated to the reconstructed images as an “alternating” tSNR level across the adjacent slices. If the tSNR map is reformatted into another plane, alternating high/low tSNR stripes are readily seen (Polimeni et al., 2016). This spatially varying tSNR pattern is therefore likely to change depending on the timing of head motion or respiration relative to the ACS acquisition and thus is expected to change across runs.

An alternative solution is to use the fast low-angle shot (FLASH) (Haase et al., 1986) method to acquire ACS data for the accelerated EPI reconstruction. FLASH ACS for accelerated EPI has been proposed (Griswold et al., 2006), and a non-interleaved version in which the data for each slice is acquired in full before moving onto the next slice has been recently demonstrated to reduce g-factor penalties in EPI reconstructions (Talagala et al., 2016). However, while it may improve tSNR consistency across runs it does not provide matching geometric distortion between the ACS data and accelerated image data, and therefore may only be appropriate in cases where the EPI distortion is small.

A recent study has employed the Fast Low-angle Excitation Echo-planar Technique (FLEET) (Chapman et al., 1987) for acquiring ACS data to calibrate GRAPPA kernels for accelerated EPI reconstructions; the FLEET acquisition is simply a reordering of the acquisition of the multi-shot EPI segments that acquires the complete set of segments within a slice before proceeding to acquire the next slice, and has been proposed as an acquisition method for fMRI (Guilfoyle and Hrabe, 2006; Kang et al., 2015; Menon et al., 1997). This acquisition approach minimizes the time interval between the acquisition of all the segments of one slice, which, when applied to acquiring accelerated EPI ACS data, minimizes sensitivity to dynamic changes occurring during the ACS acquisition (such as subject motion and respiration) to increase the robustness of the ACS data and, consequently, the PI calibration (Polimeni et al., 2016). The resulting reduction in longitudinal recovery time necessitates lower flip angles to achieve equal magnetization across segments; empirically this loss of signal in the ACS data has not prevented the FLEET ACS data from providing high-quality EPI reconstructions, even for high-resolution acquisitions. This new FLEET ACS method has been shown to improve tSNR of the acquisition and eliminate the “slice-alternating” tSNR artifact in accelerated EPI by providing robustness to subject motion and respiration related artifacts (Polimeni et al., 2016). In this work we hypothesize that FLEET may additionally remove the aforementioned inconsistency of tSNR across multiple accelerated EPI runs.

In this work we investigated the effect of autocalibration acquisition strategy on tSNR variation between multiple runs of accelerated EPI acquisitions, and tested whether FLEET ACS could reduce this variability while maintaining high-quality image reconstructions. To characterize the performance of different autocalibration methods, we employed an across-run tSNR consistency measure as well as examined changes in the spatial distribution of high-tSNR voxels across the runs.

Methods

Five healthy volunteers (3F/2M, mean age 26±4 y.o.) were scanned on a whole-body 7T scanner (Siemens Healthcare, Erlangen, Germany) using a set of seven single-shot gradient-echo EPI protocols—three with FLEET *ACS:* acceleration factor R=2,3,4, and the number of ACS lines set to 46, 90, 76, respectively; four with conventional ACS, including: a single-shot EPI ACS acquisition for $R=2$ and 48 ACS lines (*ss-EPI ACS*), and standard segmented multi-shot EPI for R=2,3,4, and 94, 90, and 88 ACS lines respectively (*ms-EPI ACS*). Protocol parameters were: TE/TR=25/2000 ms, FOV=192 mm, matrix=96×96, 39 slices, spatial resolution 2.0×2.0 mm, slice thickness 2.0 mm, flip angle 67°, bandwidth 2264 Hz/pix, echo spacing 0.53−0.57 ms (depending on R), 4 dummy scans, no partial Fourier, acquisition time approximately 2 min 10 s. For FLEET ACS protocols the excitation flip angle was 10° (with 5 preparation pulses). Additionally, three healthy subjects (2F/1M, mean age 26±2 y.o.) were scanned on a 3T scanner (MAGNETOM Tim-Trio Siemens Healthcare, Erlangen, Germany) with a set of seven protocols matching the parameters used in 7T, except for: TE/TR=30/2000 ms, FOV=240 mm, 34 slices, spatial resolution 2.5×2.5 mm, slice thickness 2.5 mm, flip angle 77°, echo spacing 0.53−0.55 ms (depending on R). Before each of the scanning sessions subjects were asked to remain still during the scans and throughout the session. Finally, an agar gel phantom was also scanned at 3T using identical protocols. All seven protocols, consisting of 60 measurements (i.e., N_{tp}=60) each, were repeated four times in a randomized order for each subject to quantify the tSNR consistency across repeated scans.

Preprocessing

Motion correction was performed for all data sets (using the MCFLIRT tool from the FSL software package, http://fsl.fmrib.ox.ac.uk/fsl/fslwiki/) with normalized correlation as a cost function and a trilinear interpolation method (the default options), using as reference the average volume taken across all the time points for each acquisition. tSNR maps were calculated as the temporal mean divided by the temporal standard deviation after linear detrending, and were generated for all acquisitions (i.e., all N_{tp}=60 time points) and for two halves of each acquisition (N_{tp}=30) in order to investigate tSNR changes occurring between separate runs as well as within a specific run. All tSNR maps were subsequently spatially smoothed in 2D with a 3-by-3 voxel Gaussian kernel to help identify spatial trends in the maps. Brain masks were created automatically (using the FSL tool BET) for each acquisition based on a mean volume previously used for motion correction, and CSF was removed using automatically obtained masks (using the FSL tool FAST, probability threshold of 0.99, only for human brain data). Multiple runs of the same protocol were then aligned to the first acquired run (using the FSL tool FLIRT) and the same transformations were applied to the corresponding brain masks and smooth tSNR maps. Spatial-mean values of tSNR were taken from within the brain masks and normalized for each session to the highest tSNR among four runs of the protocol using ss-EPI ACS in order account for differences in absolute tSNR between the subjects. In addition, the ratio of standard deviation divided by mean calculated across the normalized spatial-mean tSNR values of all runs and all subjects was used to quantify the tSNR percent variation across repeated trials for each protocol.

Relative tSNR change (ΔtSNR)

In order to investigate tSNR consistency within and across different runs of the same scan protocol and, in particular, the spatial pattern of the tSNR variations, relative tSNR change (ΔtSNR) maps were computed voxelwise as follows. For each pair of smoothed tSNR maps the ratio of the tSNR difference was divided by the tSNR sum, such that the ΔtSNR between run A and run B can be expressed by the following equation: $\Delta\text{tSNR}(\text{run}_A, \text{run}_B) = [\text{tSNR}(\text{run}_A) - \text{tSNR}(\text{run}_B)]/[\text{tSNR}(\text{run}_A) + \text{tSNR}(\text{run}_B)]$.

Relative tSNR change (ΔtSNR) is a symmetrized equivalent of the noise-to-noise ratio (NNR) introduced in earlier work by Cheng (Cheng, 2012), modified to achieve symmetry of the metric such that values fall within the range of −1 to 1 symmetrically about the 0 value. tSNR maps of halves of individual runs were used to calculate within-run ΔtSNR and tSNR maps of two different runs (aligned to the first run) were used to calculate across-run ΔtSNR for every pair of runs of the same scan protocol (six possible combinations of four runs). To quantify the range of ΔtSNR values in a way that avoids outlier values influencing the summary statistics (see Supplementary Figure 5), the full-width at half-maximum (FWHM) of the histogram of ΔtSNR values within the brain mask were calculated for each pair of runs for across-run ΔtSNR and for each run for within-run ΔtSNR. This provided a measure of the spread of values in the histograms, which were consistently uni-modal but tended to have non-Gaussian tails. In order to check for any unexpected trends in ΔtSNR with time, we calculated median values for each pair of runs.

Spatial clusters

The spatial consistency of high-tSNR regions across the runs was examined by quantifying both the overlap of high-tSNR regions across runs as well as the spatial displacement of high-tSNR regions between runs. This was accomplished by identifying clusters of high tSNR values within a given slice and run using thresholding, where the threshold was iteratively adjusted until it provided 10 clusters. The threshold search range was the 70–100th percentile of the tSNR for a given slice (because a low threshold could result in large clusters containing most of the voxels). The minimum cluster size was constrained to 9 voxels in order to avoid very small clusters corresponding to spurious, isolated peaks in the tSNR maps caused by noise. To confirm the consistency of these metrics based on these high-tSNR clusterings, we calculated cluster overlap and cluster displacement using 8 and 12 clusters as well.

The clusterings of all runs were then aligned to the first run using previously obtained registration transformations. In order to measure spatial overlap between all pairs of clusterings corresponding to pairs of runs for each protocol, Dice coefficients were calculated using the total number of voxels in two clusterings and the number of voxels which fall into their intersection. This measure ranges from 0 to 1, where 1 corresponds to the highest similarity and in our case represents an ideal overlap of two clusterings. The two top-most and two bottom-most slices were omitted from the analysis because very little or no overlap between these extremal slices are observed after alignment (see Supplementary Figure 1).

To measure potential displacements of the high-tSNR voxels cluster across two runs we calculated the average inter-cluster distance: a distance of clustering *A* from the clustering *B* and the other way around (see Supplementary Figure 2 for further explanation). Finally, the overlaps between clusterings obtained for all runs of a given protocol were calculated, and the voxel clusters having high tSNR in one, two, three and four runs were counted.

The significance of all performance metrics—including normalized tSNR, FWHM of ΔtSNR, Dice coefficient and inter-cluster distance—was tested statistically using Wilcoxon rank-sum test (non-parametric, independent variables).

Results

tSNR

Example slices of tSNR maps calculated for FLEET ACS and ms-and ss-EPI ACS reconstructed EPI data acquired at 7T with R=2 for a representative human subject are presented in Figure 1 (and analogous results for 3T human data are presented in Supplementary Figure 3). Stripes of lower and higher tSNR corresponding to adjacent slices can be seen in the sagittal reformats of the dataset reconstructed with ms-EPI ACS, and correspond to the aforementioned “slice-alternating” tSNR artifact. Note that subset of low-tSNR slices will vary from run to run of the same acquisition protocol (see Discussion for more details). The slice-alternating tSNR was not seen in time series reconstructed using ss-EPI or FLEET ACS data, as reported previously (Polimeni et al., 2016). The slice-alternating tSNR effect was not present in the 3T phantom images reconstructed using any of the ACS acquisition methods tested (Supplementary Figure 4). Mean normalized tSNR values across the brain are summarized in Table 1, with the tSNR values observed in time-series reconstructed with FLEET ACS data for both 7T and 3T acquisitions being statistically significantly higher than those reconstructed with ss-EPI ACS and ms-EPI ACS for the corresponding R factors ($p<0.01$, also see Supplementary Table 1). This could be partially due to the SNR differences in the ACS data acquired by these techniques (see Polimeni et al., 2016, and Supporting Figures 4 and 5 therein). Normalized tSNR percent variation was also larger for reconstructions using ms-EPI ACS acquisitions than for reconstructions using FLEET ACS (Table 1). Note that tSNR of the datasets acquired at 3T was higher than for those from 7T, presumably due to the larger voxel size used at 3T (2.5 mm vs. 2.0 mm) and the higher physiological noise levels at 7T (Triantafyllou et al., 2005).

Relative tSNR change (ΔtSNR)

To quantify the variability of tSNR, within-and across-run ΔtSNR maps were computed. Values of within-run ΔtSNR were relatively low and spatially uniform (Figure 2), as previously reported (Cheng, 2012), and were similar for all ACS techniques suggesting high consistency of GRAPPA reconstructions within each time series.

The across-run ΔtSNR was lower for images reconstructed with FLEET ACS than for images reconstructed with ms-EPI ACS acquisitions, as presented in both Figure 3 for our 7T data (also see Supplementary Figure 6) and in Figure 4 for our 3T data, indicating improved across-run consistency of tSNR when using reconstructions based on FLEET

ACS. In addition, across-run ΔtSNR maps calculated for ms-EPI ACS acquisitions suffered from spatial inhomogeneity effects, specifically a “slice-alternating” effect, similar to the aforementioned slice-alternating tSNR artifact, as well as patches of higher/lower values in the reconstructions based on ms-EPI ACS acquisitions. This discontinuity effect was not present at the across-run ΔtSNR maps calculated for the 3T gel phantom data (Figure 5). Visual comparison of ΔtSNR maps presented for 7T data in Figures 2 and 3 suggests that FLEET ACS with R=4 can provide across-run tSNR consistency approaching a similar level —but still lower than—the within-run tSNR consistency. Ideally the within-run and across-run tSNR consistencies would be identical.

The FWHM of within-and across-run ΔtSNR values, computed to summarize the spatial heterogeneity of the pattern of tSNR differences within and across runs, are presented in Table 1 (also see Supplementary Figure 7). Within-run ΔtSNR FWHM values were relatively low for all protocols with a tendency to be higher for data reconstructed using FLEET ACS technique (see Table 1). A significantly reduced spatial heterogeneity in across-run ΔtSNR was seen in images reconstructed using FLEET ACS or ss-EPI ACS compared to those reconstructed using ms-EPI ACS for corresponding R factors, in all data from 7T (p<0.01) as well as for data acquired at 3T (p<0.01), as summarized in Table 2. The heterogeneity observed in the 3T data was overall about two times smaller than that found for 7T data. A trend can be seen of decreasing across-run ΔtSNR heterogeneity with increasing R factor for both ACS acquisition types and both field strengths, indicating that the across-run consistency improves with higher acceleration. This also shows that the performance of the conventional ms-EPI ACS method and the proposed FLEET ACS method becomes similar for higher R factors. Interestingly, for data reconstructed using EPI ACS, the ΔtSNR heterogeneity was found to worsen as a function of time when comparing runs separated by longer time intervals, as plotted in Figure 6. This suggests that some portion of the ΔtSNR heterogeneity may be caused by longer-term effects, such as slow, gradual changes in head position occurring during the experimental session. No patterns or trends were found for median ΔtSNR values.

To test whether within-run changes in tSNR were indeed smaller than across-run changes in tSNR, the FWHM of within-run ΔtSNR values was compared to across-run ΔtSNR; these results are presented in Supplementary Table 3. In summary, the within-run tSNR changes were found to be similar to the across-run tSNR changes in the FLEET ACS data for R=2 and R=4 (p=0.91 and p=0.10) and ss-EPI ACS (p=0.41), weakly significantly higher for FLEET ACS with R=3 (p<0.05) (see Discussion for explanation), but significantly lower for all ms-EPI ACS data (p<0.01). This suggests that the main source of variability in tSNR maps between runs is related to across-scan effects rather than within-scan effects, in agreement with previous observations (Cheng, 2012).

In summary, images reconstructed with FLEET ACS outperformed those reconstructed with ms-EPI ACS for all the temporal consistency measures, but were comparable to those reconstructed with ss-EPI ACS data (albeit ss-EPI ACS data were only acquired for R=2 protocols). The across-run inconsistency increased with the increasing field strength, and was not observed in the phantom data.

Spatial clusters

Overlap between high-tSNR clusters (quantified using the Dice coefficient) was significantly higher for images reconstructed using FLEET ACS or ss-EPI ACS than for images reconstructed using ms-EPI ACS ($p<0.01$, see Supplementary Table 4), and this calculated overlap increased with the higher acceleration factor R (Table 3). The possible displacement of the high-tSNR clusters across two runs (expressed as the inter-cluster distance) was ~4 mm for images reconstructed with FLEET ACS, slightly higher for images reconstructed with ss-EPI ACS, and about twice as high (~8 mm) for images reconstructed with ms-EPI ACS (Table 3 and Supplementary Table 6). Displacement also decreased with the increasing acceleration factor for both images reconstructed with FLEET ACS and those with ms-EPI ACS. The overlap as well as the cluster displacement measure were consistently better for slices located within the bottom half of the brain (see discussion). Figure 7 summarizes the results quantifying the percentages of voxels belonging to high-tSNR clusterings in one, two, three or four runs of the same protocol. The percentage of voxels which were clustered as having high tSNR in all four runs (red in Figure 7B) was higher in images reconstructed with FLEET ACS and ss-EPI ACS than in images reconstructed with ms-EPI ACS. Example slices of two sets of overlapped clusterings obtained for four R=3 runs of images reconstructed with FLEET ACS and corresponding images reconstructed with ms-EPI ACS are also presented (Figure 7A).

Discussion

In this work we reproduced the across-run tSNR variability previously reported for conventional GRAPPA-accelerated EPI acquisitions (Cheng, 2012) and demonstrated that images reconstructed using FLEET ACS show improved across-run tSNR consistency and reduced spatial displacement of the high-tSNR regions across runs compared to images reconstructed using conventional ms-EPI ACS. Inconsistency of the tSNR occurring between different runs of the same fMRI experiment arising from signal variability or noise could strongly influence fixed-or random-effects analyses used to combine the runs, potentially leading to biased interpretation of the resulting activation maps. As we showed, FLEET ACS not only provides smoother tSNR than conventional methods, thereby decreasing spatial detection bias, but it also increases overall tSNR levels, improving sensitivity of the acquisition to detect subtle signal changes.

The ΔtSNR metric used in our study to assess tSNR variability is a modified version of the noise-to-noise ratio (NNR) presented in the earlier work by Cheng (Cheng, 2012). In order to simplify the interpretation of the results, we introduced a symmetry about 0 for the ΔtSNR values calculated between two tSNR maps by dividing the tSNR difference in each voxel by the tSNR sum. The ΔtSNR maps are useful in this context because they depict how the spatial pattern of tSNR varies between two runs. While we also summarize the change in tSNR seen across runs for quantitative comparison, these voxelwise ΔtSNR maps help to identify cases where two runs may each have the same degree of spatial variability of tSNR, but the exact spatial pattern of variability changes from one run to the next, which can impact the interpretation of the results. While the shifting pattern of tSNR across multiple runs could “average out” if runs are combined, the shifting pattern of tSNR would have a

much more serious impact on experiments where multiple tasks are presented across the runs and the fMRI responses measured in these runs are compared.

Similar to the earlier study, we found that within-run ΔtSNR was relatively low (Figure 2, Table 1) compared to across-run ΔtSNR of data reconstructed with ms-EPI ACS method (Figures 3 and 4, Table 1, Supplementary Table 3), indicating decreased tSNR consistency between two separate runs of the same protocol in an experimental session. The FWHM of within-run ΔtSNR values was found weakly significantly higher than FWHM of across-run ΔtSNR for FLEET ACS R=3 data, however the FWHM of across-run ΔtSNR values were much more spread (larger standard deviations) for all EPI ACS data than for FLEET ACS data (see Table 1), and significantly higher than FWHM of within-run ΔtSNR (see Supplementary Table 3). This suggests that tSNR inconsistency originates from the independent autocalibration of the GRAPPA reconstruction coefficients for each run, and the ACS data acquired at the beginning of each run affecting the performance of GRAPPA reconstruction kernel, rather than from any effect occurring in the actual image data acquisition (such as drift) causing incompatibility between the kernel and the data over a short period of time. A similar conclusion was reached by Cheng from experiments that reconstructed offline the time-series data from two different runs using the same calibration data for each reconstruction (Cheng, 2012).

Because the GRAPPA reconstruction coefficients are regenerated for each run, the observed tSNR inconsistency across runs is unlikely to be caused by subject motion occurring throughout the experimental session with respect to the strongly spatially varying B_1^- fields (inhomogeneous receive sensitivity profiles), which would be expected to cause both within- and across-run tSNR variance. The across-run ΔtSNR FWHM values obtained for data reconstructed using FLEET ACS were similar to within-run ΔtSNR, and for FLEET ACS with R=3 across-run ΔtSNR FWHM was significantly lower than within-run ΔtSNR FWHM (p=0.02). This last, surprising result could possibly be explained by the fact that tSNR maps used to quantify within-run ΔtSNR were calculated using only half (30) time points. This caused the effects of even slight head motion occurring within the run to be more severe in these tSNR maps than in tSNR maps used to calculate across-run ΔtSNR where full time series (60 time points) were included.

In slice-interleaved acquisitions, anatomically adjacent slices of the segmented EPI ACS acquisition may be acquired at different phases of the respiratory cycle, leading to discontinuous tSNR in the slice direction. Since two repeated runs of the same protocol are likely to initiate the ACS data acquisition at different phases of the subject's respiratory cycle, and the rate of the cycle is not expected to be perfectly constant over time, the affected subset of slices that exhibit lower tSNR will differ between the two runs, causing a spatial mismatch in the spatial pattern of tSNR in the two runs that can be seen in ΔtSNR maps as between-slice discontinuity. This effect does not occur in images reconstructed using the ACS acquired with single-shot EPI (ss-EPI ACS), which in this study reached tSNR levels and consistency closest to the FLEET ACS reconstructions. However, typical implementations of the ss-EPI ACS technique only allow it to be used with R=2 acceleration factor, presumably because for low acceleration the effective echo spacing between the ACS and accelerated data will be roughly similar, leading to a more approximate distortion match

between the ACS and accelerated data. For higher acceleration factors of $R \geq 3$, the distortion mismatch becomes more severe, preventing the ss-EPI ACS technique from being used for ACS data. Both breath-holding during the ~20 s ms-EPI ACS acquisition has been previously shown to reduce the "slice-alternating" effect within the single scan (Polimeni et al., 2016).

Here we demonstrated that this improved spatial smoothness of tSNR has an important impact on tSNR consistency between separate runs of the same scan, as reflected in the smooth ΔtSNR maps corresponding to runs reconstructed with FLEET ACS shown in Figures 3 and 4. The derived ΔtSNR maps corresponding to acquisitions reconstructed using ms-EPI ACS from both 7T and 3T human data were strongly affected by the "slice-alternating" discontinuous tSNR artifact (Figures 3 and 4). This effect can be in part attributed to respiratory-driven chest motion, which can differentially affect EPI segments of a segmented EPI ACS acquisition acquired at different phases of subject's respiratory cycle and corrupts the GRAPPA kernel fitting in affected slices, as previously demonstrated (Polimeni et al., 2016).

It should be noted that the ΔtSNR maps presented in Figure 3 and 4 were taken from different run pairs and therefore the effects other than those due to the ACS data, such as head motion occurring during the time-series acquisition, could impact tSNR and cause its across-run variability. In the example map presented in Figure 3 comparing tSNR for an FLEET-ACS $R=3$ acquisition in one subject between run 2 to run 4, the ΔtSNR map demonstrates that the tSNR was overall lower in run 2 than for run 4, however the ΔtSNR map exhibits a high degree of spatial uniformity reflecting that runs 2 and 4 have similar spatial pattern of tSNR—indeed, when comparing these runs the ΔtSNR map is almost entirely blue (indicating a $\Delta tSNR < 0$), whereas inspection of similar comparisons from the ms-EPI ACS data in the bottom panel of Fig. 3 shows ΔtSNR maps with a mixture of red and blue regions indicating differing spatial patterns of tSNR and therefore lower across-run tSNR consistency between the two runs. As a whole, the trends and statistical tests confirmed that there is an effect of ACS acquisition strategy on the tSNR and tSNR variability and FLEET ACS provides a substantial improvement in across-run tSNR consistency (also see Supplementary Figure 6).

The previous study investigating across-run tSNR variation in accelerated EPI acquisitions performed quantitative analysis on a slice-wise manner (Cheng, 2012). However, in case of the human data, such an approach could potentially skew the resulting values because slices containing only very bottom or very top parts the brain tend to exhibit relatively higher tSNR variability across runs, potentially due to strong B_0 nonuniformity and/or spin history effects seen in these outermost boundary slices. In our work we performed ΔtSNR calculations on a whole volume of the acquired data, skipping two top and two bottom slices for each brain.

The metric quantifying the range of ΔtSNR values, i.e., the FWHM of the ΔtSNR histogram, was chosen based on examination of the ΔtSNR value distributions and the tails of these distributions, which varied substantially between different acquisitions, posing a challenge to selecting an appropriate range of values that could successfully discount outliers in all

cases. The outliers rejected using a percentile range tended to yield slightly different outcomes in the datasets reconstructed with FLEET ACS, where the identified outliers tended to appear as spurious peaks in the tSNR falling mostly with CSF regions, compared to those reconstructed with ss-or ms-EPI ACS, where the identified outliers often appeared as spatial patches of very high/low tSNR within the slices (as shown in Supplementary Figure 5). Therefore, the FWHM approach was adopted to be less arbitrary and also the most intuitive to interpret.

We examined the FWHM ΔtSNR values and found less spatial heterogeneity in images reconstructed with FLEET ACS than for those reconstructed with ms-EPI ACS, indicating lower tSNR variability between the runs while using FLEET ACS (Table 1), and also that spatial heterogeneity decreases with the increasing acceleration factor *R*. Across-run tSNR inconsistency increased with the field strength, which was reflected in generally narrower ranges of ΔtSNR found in 3T than in 7T data. These results provide a quantitative confirmation of advantages of reconstructions using FLEET ACS seen through visual assessment of the ΔtSNR maps. The trend for across-run tSNR variability to improve with increasing acceleration factor *R* was expected for compliant subjects (who largely remain still during the scan). For patient populations prone to head movement, this trend may not hold, since ms-EPI ACS is extremely vulnerable to head motion—and the vulnerability becomes greater with higher acceleration factors which necessitate higher segmentation factors and more shots—while FLEET ACS has been shown to be robust (Polimeni et al., 2016); thus for non-compliant subjects or in cases of overt motion (Cardoso et al., 2016) ms-EPI ACS is expected to perform worse for higher acceleration factors. It can be also partly explained by the increased thermal noise contributions in the accelerated data relative to physiological noise when using higher *R* factors, which causes the spatial profile of tSNR to become more smoothly varying in space (Triantafyllou et al., 2011; Wald and Polimeni, 2016).

The time interval separating pairs of compared runs also affected spatial heterogeneity of tSNR differences for data reconstructed with EPI ACS, and stronger effects were seen for scans acquired further apart in time (Figure 6). This suggests the existence of additional effects impacting across-run tSNR consistency (e.g. small, slow shifting of head position) that accumulate with time.

Unlike the previous study (Cheng, 2012), we did not find a noticeable tSNR inconsistency between different runs of scans acquired for a gel phantom at 3T (Figure 5 and Supplementary Figure 4). Using a volume-based approach instead of a slice-based approach could potentially contribute to this difference. More likely, it suggests that the inconsistency reported for a phantom in the previous work was caused by additional spatial effects that accumulate with time (since in this previous work 1st and 10th runs, separated by a long time interval, were compared) which were not present in our data. From the perspective of this study, the lack of or the minimal across-run tSNR inconsistency in the phantom data confirms the hypothesis about tSNR variation being related to dynamic changes seen in subjects such as bulk head or respiratory motion.

The across-run tSNR inconsistency seen in images reconstructed with the conventional ms-EPI ACS could impact the consistent detection and localization of BOLD activation across runs and subjects. If regions of high and low tSNR shift between runs, a true activation could be missed in runs in which the activation occurs in a region of low tSNR, and therefore this inconsistency would not only introduce additional variability into the comparison of activation maps across runs but could also potentially cause a detection bias whose spatial pattern shifts with time, leading to misinterpretation of the observed activation maps. The detection power of fMRI experiment directly depends on tSNR of the acquisition (Cheng, 2012; Murphy et al., 2007) and can be calculated straightforwardly as: $p = erfc(\mathrm{tSNR} \cdot eff \cdot \sqrt{N/8})$, where *erfc* is the complementary error function, *eff* is the effect size (activation related signal change divided by the baseline signal) and *N* is a total number of degrees of freedom in the time-series data (assuming that task was performed in half of them). Using this expression, we can see the impact of the changes detection power expected based on the observed changes in tSNR across runs when using an image reconstruction using the conventional ms-EPI ACS. For the example, assuming a typical effect size of 1% and an acquisition including 100 time points, a tSNR decrease of 10%, from 40 to 36 (realistic values obtained in this study for data acquired at 7T, see Figure 1), will result in significance level decrease from p=0.046 to p=0.072. Thus a voxel exhibiting this effect size would be counted as a significant activation in one run and a non-significant activation in the other due to a flaw in conventional image reconstruction strategies.

The results of the clustering-based measures of spatial tSNR consistency and shifting patterns of tSNR introduced in this study followed the same trends as those obtained based on ΔtSNR maps (Table 1, Figure 7). Both overlap between high-tSNR clusters (Dice coefficient) and high-tSNR cluster displacement (inter-cluster distance) demonstrated the advantages of image reconstructions using FLEET ACS acquisitions over those using conventional ms-EPI ACS, with the highest acceleration factor acquisitions yielding the most consistent maps. This could be clearly seen in the comparison of the average high-tSNR cluster displacement, which was doubled in the R=2 case between images reconstructed with ms-EPI ACS compared with those reconstructed with FLEET ACS—a shift of high-tSNR regions up to 8 mm was detected in reconstructions using ms-EPI ACS versus a 4 mm shift in reconstructions using FLEET ACS. Slices located within the bottom half of the brain consisting of fewer voxels had better cluster overlap and displacement measures. In addition, higher improvement of both consistency measures was found in the mid/bottom part of the brain, which may be explained by the larger numbers of brain voxels included in these central slices compared to the slices located near the top or bottom of the brain.

Our use of spatial clusters to perform this analysis was inspired in part by the cluster analysis commonly used in fMRI. Correction for multiple comparisons in conventional fMRI data analysis often employs clustering approaches to discard false positives to help identify and locate genuine activations (Beckmann et al., 2006; Friston et al., 1994; Hagler et al., 2006). While our use of clusters was motivated by the need to track how regions of high tSNR shift across runs, observations of contiguous regions of low and high tSNR seen in the data (e.g., in Figure 1) justify our use of high-tSNR clusters. Furthermore, because

tSNR may change globally across runs even if the spatial patterns remain constant, we adapted our tSNR threshold that defined the high-tSNR clusters to each run. By ensuring that the same number of clusters was identified in each run, and the cluster sizes were small, we could compute the overlap of clusters between runs as a measure how far the high-tSNR regions moved. While the absolute overlap will be a function of the tSNR threshold, because this threshold was set in a consistent way across all runs the relative changes in overlap provided a meaningful measure of how each ACS acquisition strategy impacts across-run tSNR variability.

Because of the spatial correlation of physiological noise (Triantafyllou et al., 2006), the different physiological noise levels in different tissue classes such as gray matter, white matter, and CSF (Bodurka et al., 2007), and the smoothly varying image SNR that is largely a function of the receiver coil sensitivity (Triantafyllou et al., 2011), it is expected that tSNR should vary relatively smoothly over space. In some cases, we identified high-tSNR clusters in white matter regions (Figure 7A), which, due to the relatively low-levels of physiological noise found in cerebral white matter, tend to have relatively high tSNR compared to adjacent gray matter. Interestingly, the tSNR differences between different tissue classes were largely absent in ΔtSNR maps (which are essentially a ratio of two tSNR maps), therefore the spatial patterns of tSNR changes from run to run appear to be unrelated to the anatomy and tissue type (see Figures 3 and 4).

Displacement of the high-tSNR regions across different runs of the same scan protocol can be partially related to the aforementioned “slice-alternating” tSNR artifact. In order to compute tSNR consistency maps between pairs of runs, these multiple runs have to be spatially aligned to one another using a rigid body transformation. The “slice-alternating” tSNR effect leads to the adjacent slices having significantly varying tSNR levels, which, after alignment (for example tilting or shifting the volume along the slice-axis), low-tSNR slices of one run can be partially resampled into high-tSNR slices of the other run and vice versa, introducing patches of high and low ΔtSNR values within a given slice after alignment. Since slice tSNR discontinuity differs between the runs, this effect will impact each run differently, providing a potential source of tSNR changes observed within a particular slice.

Several recent studies have investigated new methods for acquiring ACS data for GRAPPA reconstructions, and these modern, robust ACS acquisitions may also provide improved tSNR consistency across runs. A FLASH-based approach (critically, 2D FLASH with no slice interleaving, therefore equivalent to FLEET but with the number of shots equal to the number of phase encoding lines rather than the acceleration factor) has been shown to reduce g-factor penalties in EPI reconstructions (Griswold et al., 2006; Talagala et al., 2016; Vu et al., 2014) similarly to FLEET ACS (Polimeni et al., 2016). Recent work by Talagala et al. has also shown that g-factor values calculated for FLASH ACS data remain constant and low over a wide image SNR range of the ACS data, while for EPI ACS data g-factor increases rapidly with increasing SNR (Talagala et al., 2016). However, the FLASH ACS data are undistorted, whereas the accelerated EPI has distortions, therefore the FLASH ACS data are not distortion-matched to the image data, which limits applicability of this technique to cases of small/negligible distortion. In addition, images reconstructed using

FLASH ACS have been shown to have similar or lower tSNR than those using FLEET ACS (Polimeni et al., 2016). Readout-segmented EPI was recently proposed as ACS data for GRAPPA reconstructions of accelerated EPI data and was shown to significantly improve ghosting levels in reconstructed data compared to conventional ms-EPI ACS methods (Baron and Beaulieu, 2016); this method used distortion-matched ACS segments allowing reduction of motion-related artifacts (including respiratory and eye motion) in ms-EPI ACS based reconstructions, however it assumed GRAPPA kernel consistency across segments even in the presence of motion. In addition, using this new readout-segmented ACS method did not improve tSNR of reconstructed data compared to ss-EPI ACS. In this work we showed that FLEET ACS not only increased run-to-run tSNR consistency of the scans, but also improved the overall tSNR values (see Table 1) compared to ms-EPI and more importantly ss-EPI ACS ($p<0.01$, see Supplementary Tables 1, 2, 3 and 4 for more details). This could potentially be a consequence of low excitation flip angles decreasing the SNR of the FLEET calibration data (Polimeni et al., 2016, Supporting Material), as it has been shown that, seemingly paradoxically, lower SNR_0 of ACS data has a regularization effect and therefore can increase the tSNR of the reconstructed data (Ding et al., 2015; Polimeni et al., 2016; Sodickson, 2000). Thus, the somewhat lower SNR_0 of FLEET ACS data compared to ms-EPI ACS data may not be a disadvantage per se. However, over-regularizing the GRAPPA kernel fit through further lowering the SNR_0 of the ACS data may increase residual aliasing (Polimeni et al., 2016, Supporting Material). The amount of explicit Tikhonov regularization applied when computing GRAPPA coefficients during kernel training may need to be controlled, reduced if using ACS data with low SNR_0 and increased for high SNR_0 data, to avoid over-/under-regularization. Despite a comparable across-run quality of ACS data using FLEET, it is still recommended to acquire ACS data at the beginning of each run as a cumulative subject motion could gradually decrease applicability of GRAPPA kernels calculated at the beginning of the scanning session.

Conclusions

In this study we show that FLEET ACS technique can reduce across-run variability of tSNR in accelerated EPI time-series data and therefore increase sensitivity of BOLD fMRI measurements. The FLEET ACS technique is less vulnerable to subject motion and respiration effects, and therefore the resulting tSNR of the FLEET ACS reconstructions is less influenced by the behavior of the subject. This reduced variability of tSNR is expected to yield a direct positive impact on both single-subject and group analyses of fMRI data.

Supplementary Material

Refer to Web version on PubMed Central for supplementary material.

Acknowledgments

We thank Dr. Oliver Hinds for valuable discussions, Mr. Ned Ohringer for recruiting the subjects and participating in acquiring the data, and Drs. Thomas Witzel, Cris LaPierre and Boris Keil for 7T scanning support. Additional support for this research was provided in part by the NIH National Institute for Biomedical Imaging and Bioengineering (P41-EB015896, K01-EB011498, and R01-EB019437) and by the MGH/HST Athinoula A. Martinos Center for Biomedical Imaging, and was made possible by the resources provided by Shared Instrumentation Grants S10-RR023401, S10-RR019307, S10-RR023043, S10-RR019371, and S10-RR020948.

References

Baron CA, Beaulieu C. Motion robust GRAPPA for echo-planar imaging. Magn Reson Med. 2016; 75:1166–1174. DOI: 10.1002/mrm.25705 [PubMed: 25920076]

Beckmann CF, Jenkinson M, Woolrich MW, Behrens TEJ, Flitney DE, Devlin JT, Smith SM. Applying FSL to the FIAC data: Model-based and model-free analysis of voice and sentence repetition priming. Hum Brain Mapp. 2006; 27:380–391. DOI: 10.1002/hbm.20246 [PubMed: 16565953]

Bianciardi M, Fukunaga M, van Gelderen P, Horovitz SG, de Zwart JA, Shmueli K, Duyn JH. Sources of functional magnetic resonance imaging signal fluctuations in the human brain at rest: a 7 T study. Magn Reson Imaging. 2009; 27:1019–1029. DOI: 10.1016/j.mri.2009.02.004 [PubMed: 19375260]

Bodurka J, Ye F, Petridou N, Murphy K, Bandettini PA. Mapping the MRI voxel volume in which thermal noise matches physiological noise-Implications for fMRI. NeuroImage. 2007; 34:542–549. DOI: 10.1016/j.neuroimage.2006.09.039 [PubMed: 17101280]

Cardoso PL, Polimeni JR, Poser BA, Barth M, Trattnig S, Robinson SD. A comparison of time-series SNR and Nyquist ghosting with different parallel imaging autocalibration acquisition schemes in 7 T fMRI with a chin task. Proc Intl Soc Mag Reson Med. 2016; 24:3726.

Chapman B, Turner R, Ordidge RJ, Doyle M, Cawley M, Coxon R, Glover P, Mansfield P. Real-time movie imaging from a single cardiac cycle by NMR. Magn Reson Med. 1987; 5:246–54. [PubMed: 3431393]

Cheng H. Variation of noise in multi-run functional MRI using generalized autocalibrating partially parallel acquisition (GRAPPA). J Magn Reson Imaging. 2012; 35:462–470. DOI: 10.1002/jmri.22891 [PubMed: 22069162]

de Zwart JA, van Gelderen P, Golay X, Ikonomidou VN, Duyn JH. Accelerated parallel imaging for functional imaging of the human brain. NMR Biomed. 2006; 19:342–351. DOI: 10.1002/nbm.1043 [PubMed: 16705634]

de Zwart JA, Van Gelderen P, Kellman P, Duyn JH. Application of sensitivity-encoded echo-planar imaging for blood oxygen level-dependent functional brain imaging. Magn Reson Med. 2002; 48:1011–1020. DOI: 10.1002/mrm.10303 [PubMed: 12465111]

Ding Y, Xue H, Ahmad R, Chang TC, Ting ST, Simonetti OP. Paradoxical effect of the signal-to-noise ratio of GRAPPA calibration lines: A quantitative study. Magn Reson Med. 2015; 74:231–239. DOI: 10.1002/mrm.25385

Friston KJ, Worsley KJ, Frackowiak RSJ, Mazziotta JC, Evans AC. Assessing the Significance of Focal Activations Using their Spatial Extent. Hum Brain Mapp. 1994; 1:210–220. [PubMed: 24578041]

Griswold MA, Breuer F, Blaimer M, Kannengiesser S, Heidemann RM, Mueller M, Nittka M, Jellus V, Kiefer B, Jakob PM. Autocalibrated coil sensitivity estimation for parallel imaging. NMR Biomed. 2006; 19:316–324. DOI: 10.1002/nbm.1048 [PubMed: 16705632]

Griswold MA, Jakob PM, Chen Q, Goldfarb JW, Manning WJ, Edelman RR, Sodickson DK. Resolution enhancement in single-shot imaging using simultaneous acquisition of spatial harmonics (SMASH). Magn Reson Med. 1999; 41:1236–1245. DOI: 10.1002/(SICI)1522-2594(199906)41:6<1236::AID-MRM21>3.0.CO;2-T [PubMed: 10371457]

Griswold MA, Jakob PM, Heidemann RM, Nittka M, Jellus V, Wang J, Kiefer B, Haase A. Generalized autocalibrating partially parallel acquisitions (GRAPPA). Magn Reson Med. 2002; 47:1202–10. DOI: 10.1002/mrm.10171 [PubMed: 12111967]

Guilfoyle DN, Hrabe J. Interleaved snapshot echo planar imaging of mouse brain at 7.0 T. NMR Biomed. 2006; 19:108–115. DOI: 10.1002/nbm.1009 [PubMed: 16411168]

Haase A, Frahm J, Matthaei D, Hänicke W, Merboldt KD. FLASH imaging: rapid NMR imaging using low flip-angle pulses. J Magn Reson imaging. 1986; 67:258–266. DOI: 10.1016/j.jmr.2011.09.021

Hagler DJ, Saygin AP, Sereno MI. Smoothing and cluster thresholding for cortical surface-based group analysis of fMRI data. NeuroImage. 2006; 33:1093–1103. DOI: 10.1016/j.neuroimage.2006.07.036 [PubMed: 17011792]

Kang D, Sung Y, Kang C. Fast Imaging Technique for fMRI: Consecutive Multishot Echo Planar Imaging Accelerated with GRAPPA Technique. Biomed Res Int. 2015; 2015 ID: 394213.

Krüger G, Kastrup A, Glover GH. Neuroimaging at 1.5 T and 3.0 T: Comparison of oxygenation-sensitive magnetic resonance imaging. Magn Reson Med. 2001; 45:595–604. DOI: 10.1002/mrm.1081 [PubMed: 11283987]

Menon RS, Thomas CG, Gati JS. Investigation of BOLD contrast in fMRI using multi-shot EPI. NMR Biomed. 1997; 10:179–82. doi: 10.1002/(SICI)1099-1492(199706/08)10:4/5<179::AID-NBM463>3.0.CO;2-X [pii]. [PubMed: 9430345]

Murphy K, Bodurka J, Bandettini Pa. How long to scan? The relationship between fMRI temporal signal to noise ratio and necessary scan duration. NeuroImage. 2007; 34:565–74. DOI: 10.1016/j.neuroimage.2006.09.032 [PubMed: 17126038]

Polimeni JR, Bhat H, Witzel T, Benner T, Feiweier T, Inati SJ, Renvall V, Heberlein K, Wald LL. Reducing sensitivity losses due to respiration and motion in accelerated echo planar imaging by reordering the autocalibration data acquisition. Magn Reson Med. 2016; 75:665–679. DOI: 10.1002/mrm.25628 [PubMed: 25809559]

Pruessmann KP, Weiger M, Scheidegger MB, Boesiger P. SENSE: sensitivity encoding for fast MRI. Magn Reson Med. 1999; 42:952–62. [PubMed: 10542355]

Setsompop K, Feinberg DA, Polimeni JR. Rapid brain MRI acquisition techniques at ultra-high fields. NMR Biomed. 2016; 29:1198–1221. DOI: 10.1002/nbm.3478 [PubMed: 26835884]

Sodickson DK. Tailored SMASH image reconstructions for robust in vivo parallel MR imaging. Magn Reson Med. 2000; 44:243–251. DOI: 10.1002/1522-2594(200008)44:2<243::AID-MRM11>3.0.CO;2-L [PubMed: 10918323]

Sodickson DK, Manning WJ. Simultaneous acquisition of spatial harmonics (SMASH): fast imaging with radiofrequency coil arrays. Magn Reson Med. 1997; 38:591–603. [PubMed: 9324327]

Talagala SL, Sarlls JE, Liu S, Inati SJ. Improvement of temporal signal-to-noise ratio of GRAPPA accelerated echo planar imaging using a FLASH based calibration scan. Magn Reson Med. 2016; doi: 10.1002/mrm.25846

Triantafyllou C, Hoge RD, Krueger G, Wiggins CJ, Potthast A, Wiggins GC, Wald LL. Comparison of physiological noise at 1.5 T, 3 T and 7 T and optimization of fMRI acquisition parameters. NeuroImage. 2005; 26:243–250. DOI: 10.1016/j.neuroimage.2005.01.007 [PubMed: 15862224]

Triantafyllou C, Hoge RD, Wald LL. Effect of spatial smoothing on physiological noise in high-resolution fMRI. NeuroImage. 2006; 32:551–557. DOI: 10.1016/j.neuroimage.2006.04.182 [PubMed: 16815038]

Triantafyllou C, Polimeni JR, Keil B, Wald LL. Coil-to-coil physiological noise correlations and their impact on functional MRI time-series signal-to-noise ratio. Magn Reson Med. 2016; doi: 10.1002/mrm.26041

Triantafyllou C, Polimeni JR, Wald LL. Physiological noise and signal-to-noise ratio in fMRI with multichannel array coils. NeuroImage. 2011; 55:597–606. DOI: 10.1016/j.neuroimage.2010.11.084 [PubMed: 21167946]

Vu AT, Moeller S, Auerbach E, Ugurbil K, Yacoub E. GRE reference scan for robust reconstruction of high resolution slice and in-plane accelerated 2D GE EPI at 7T. Proc Intl Soc Mag Reson Med. 2014; 22:1414.

Wald LL. The future of acquisition speed, coverage, sensitivity, and resolution. NeuroImage. 2012; 62:1221–1229. DOI: 10.1016/j.neuroimage.2012.02.077.The [PubMed: 22421052]

Wald LL, Polimeni JR. Impacting the effect of fMRI noise through hardware and acquisition choices — Implications for controlling false positive rates. NeuroImage. 2016; doi: 10.1016/j.neuroimage.2016.12.057

Wald LL, Polimeni JR. Introduction to acquisition methods: High-Speed, High-Resolution Acquisitions, in: Brain Mapping: An Encyclopedic Reference. Elsevier Inc. 2015; :103–116. DOI: 10.1016/B978-0-12-397025-1.00011-7

Highlights

- Improved across-run tSNR consistency using FLEET ACS reconstruction vs. ms-EPI ACS
- High-tSNR cluster displacement decreased by factor of two by using FLEET ACS
- FLEET ACS reconstructed data increases sensitivity of BOLD fMRI measurements

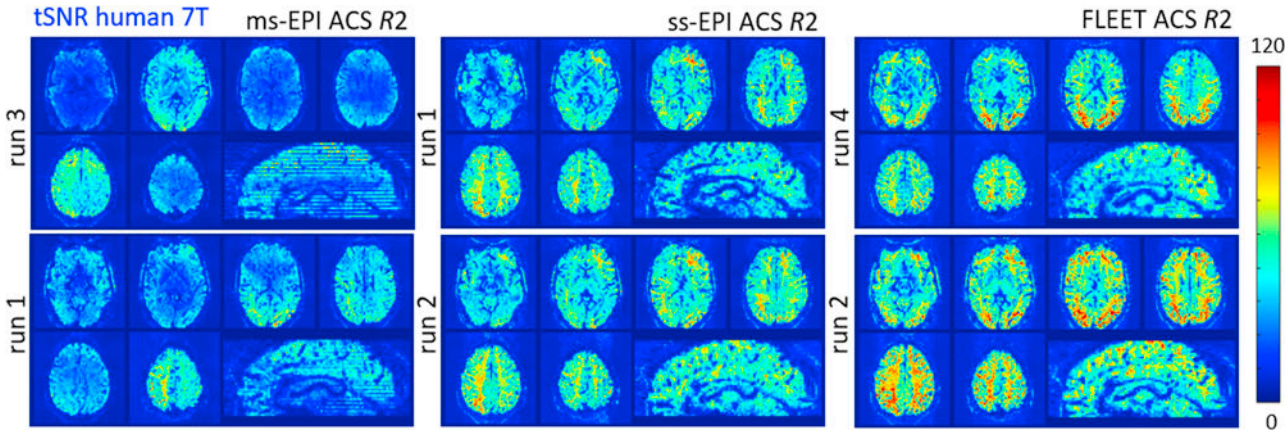

Figure 1.

tSNR maps shown in the native axial views and sagittal reformats calculated for the two runs with the *lowest overall tSNR* of ms-EPI ACS, ss-EPI ACS and FLEET ACS acquisitions with acceleration factor R=2, acquired on one subject at 7T.

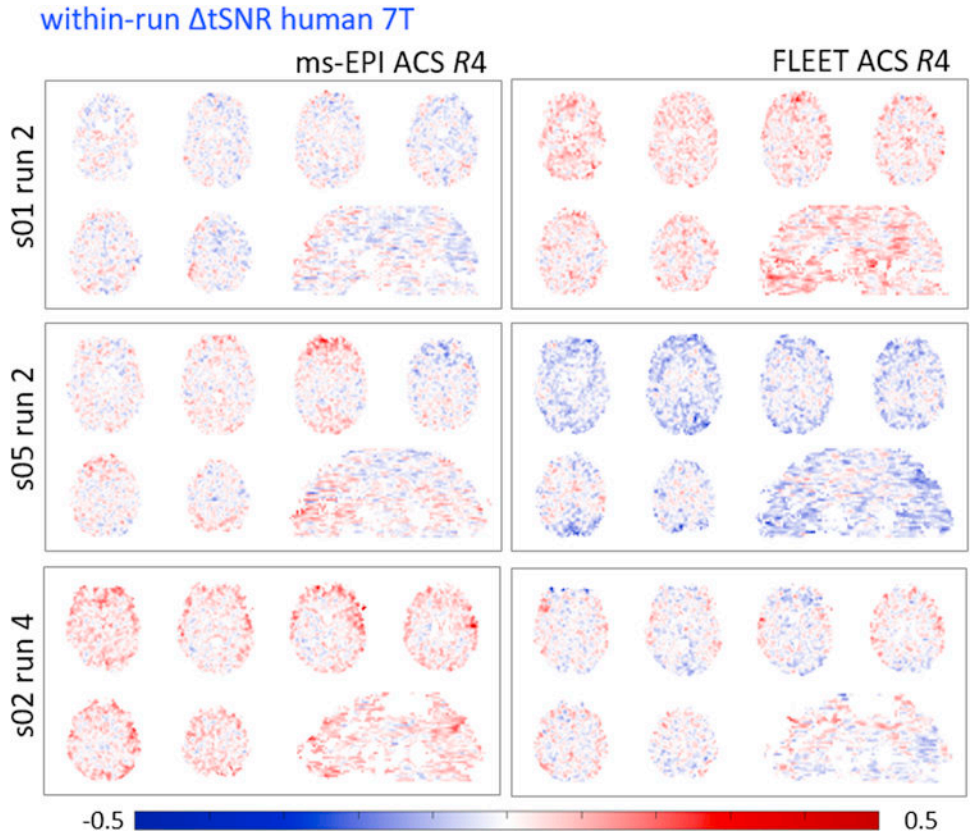

Figure 2.

Within-run ΔtSNR maps calculated between two halves of runs acquired at 7T for the same subject using ms-EPI ACS and FLEET ACS data, acceleration factor *R*=4. The full range of values [−1,1] are displayed on a truncated range [−0.5,0.5] for visualization purposes. Perfect consistency between the first and second halves of the run corresponds to a within-run ΔtSNR of 0, whereas higher or lower values indicate that the first half or second half of the run had higher or lower tSNR, respectively. The run number and subject number for each comparison are provided at left.

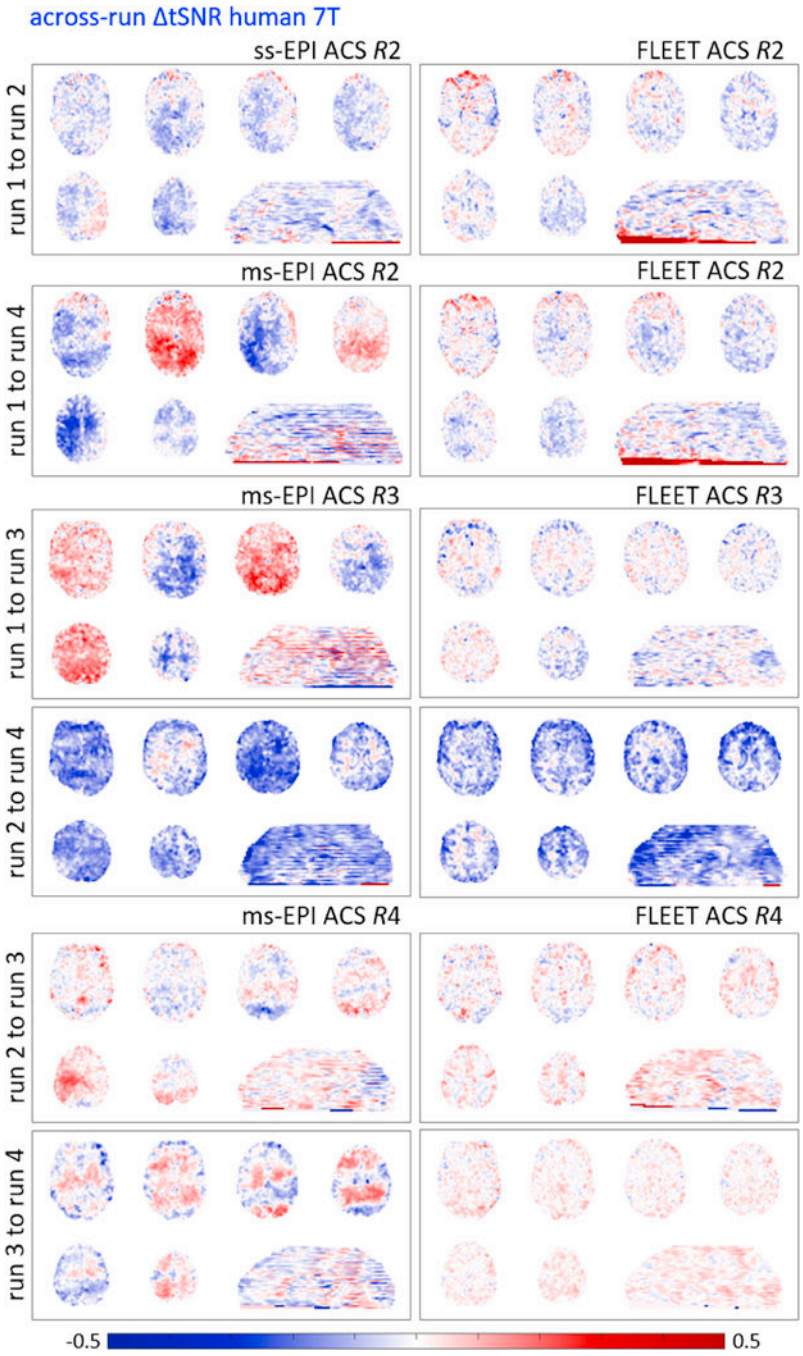

Figure 3.

Example native axial views and sagittal reformats of the across-run ΔtSNR maps calculated between different runs of the same protocol acquired for a human subject at 7T using EPI ms-EPI ACS (left) and FLEET ACS (right), with different acceleration factors. The full range of values [−1,1] are displayed on a truncated range [−0.5,0.5] for visualization purposes. Perfect consistency corresponds to a ΔtSNR of 0, whereas higher or lower values indicate that run *A* exhibits higher or lower tSNR than run *B*, respectively. The run numbers

for each comparison (e.g., run 1 to run 2 indicating comparison of run 1 of 4 to run 2 of 4) are provided at left. Each map corresponds to a pair of separate scans.

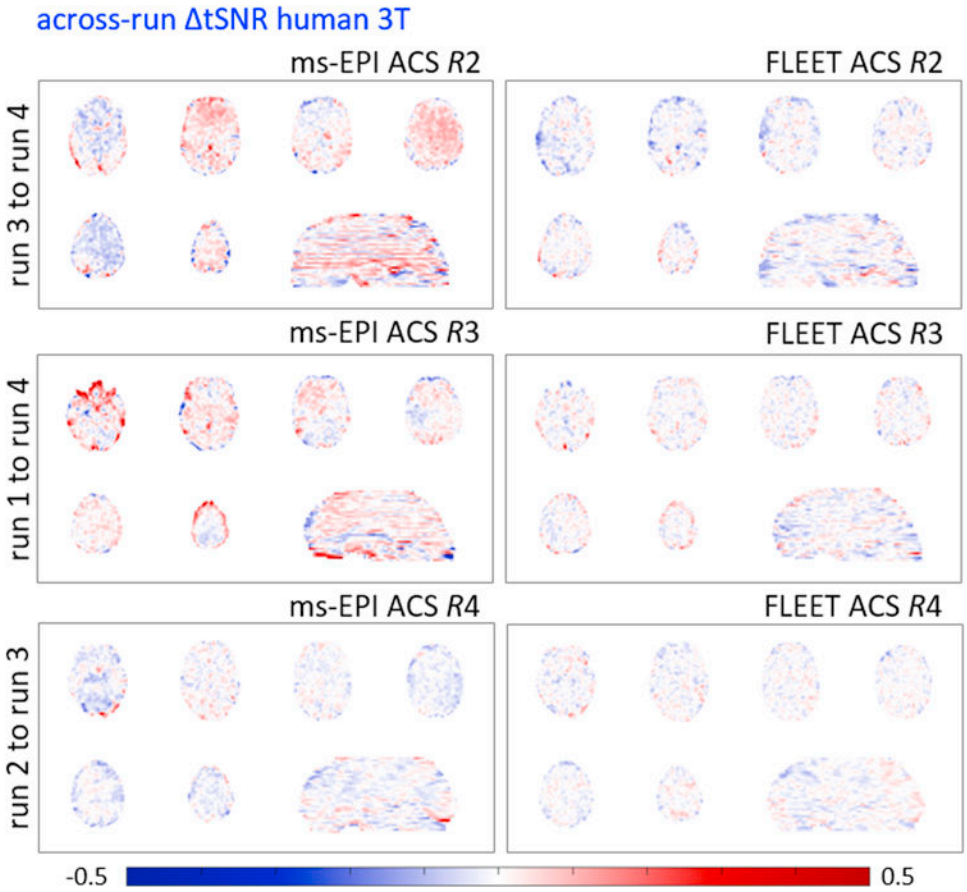

Figure 4.

Across-run ΔtSNR maps calculated between different runs of the same protocol acquired on a human subject at 3T using ms-EPI ACS (left) and FLEET ACS (right), with different acceleration factors. The full range of values [−1,1] are displayed on a truncated range [−0.5,0.5] for visualization purposes. Each map corresponds to a pair of repeated scans.

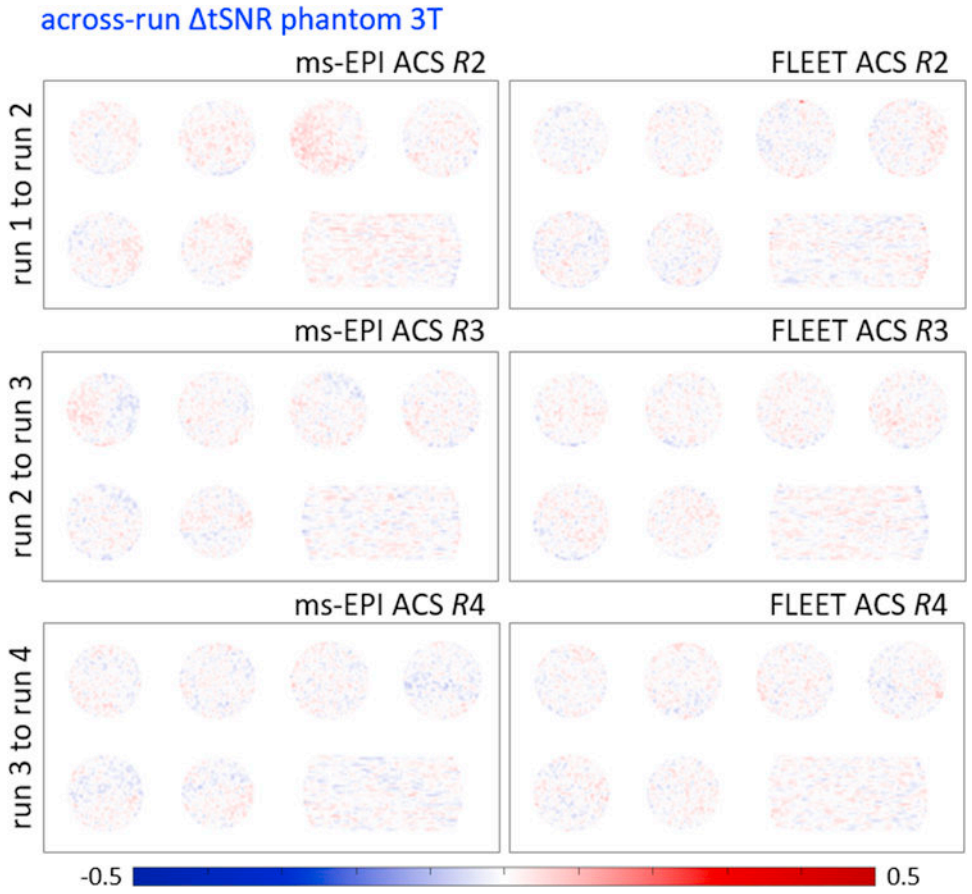

Figure 5.

Example views of the across-run ΔtSNR maps calculated between different runs of the same acquisition on a spherical, agar gel phantom at 3T using ms-EPI ACS (left) and FLEET ACS (right), with different acceleration factors. The full range of values [−1,1] are displayed on a truncated range [−0.5,0.5] for visualization purposes. The across-run consistency of the phantom data is markedly higher than what is seen in the human data.

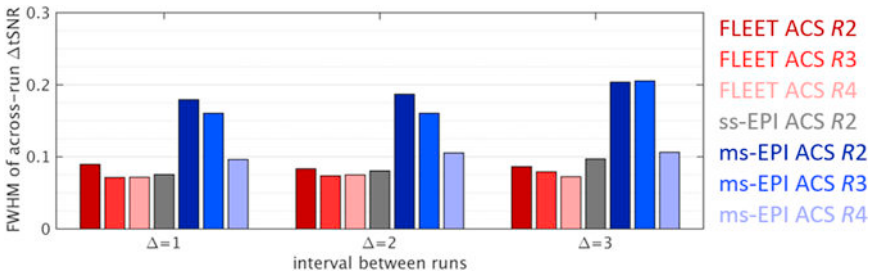

Figure 6.

Spatial heterogeneity of tSNR maps compared between runs, quantified by the FWHM of the histogram of ΔtSNR values within the brain mask, plotted as a function of time interval separating the runs. A broader range of across-run ΔtSNR values indicates higher spatial heterogeneity of the tSNR change between runs. The FWHM of ΔtSNR values, and therefore the difference in the spatial patterns of tSNR, grows as runs are acquired further apart in time.

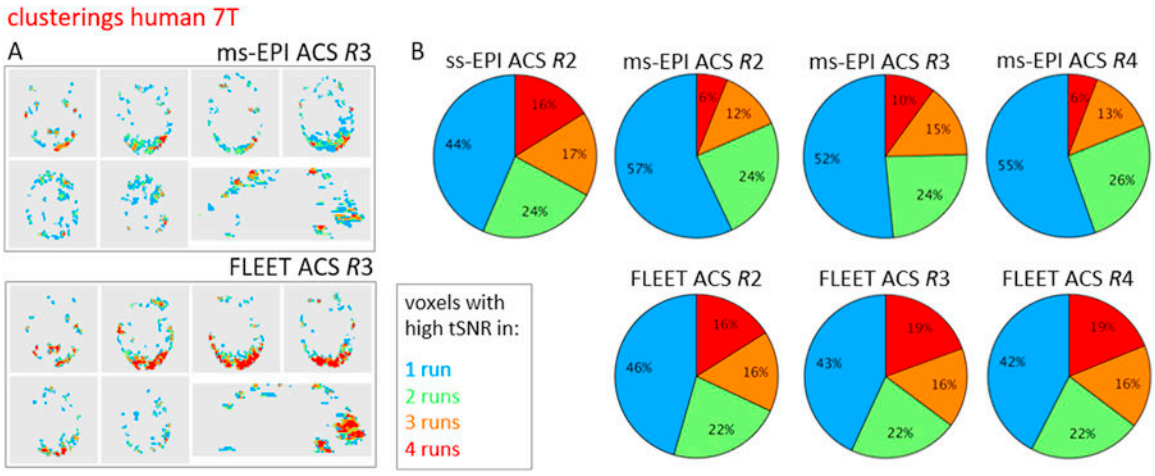

Figure 7.

(A) Example native axial views and sagittal reformats of two sets of clusterings obtained for four runs from images reconstructed using either FLEET ACS or ms-EPI ACS. (B) A summary of the percentages of voxels belonging to high-tSNR regions in one, two, three or four runs of the same protocol. In the images reconstructed with FLEET ACS there is a greater percentage of voxels that is consistently within high-tSNR regions across all four runs compared to the reconstructions using ss-EPI ACS or ms-EPI ACS.

Table 1

Summary of the quantitative measures used to compare within-and across-run tSNR variation between different protocols taken from data acquired at 7T and 3T in human subjects; the normalized tSNR averaged over the brain mask and the normalized tSNR percent variation; the FWHM of the histogram of within-and across-run ΔtSNR values; reported mean and standard deviation (±) values were calculated across all runs (tSNR and within-run ΔtSNR) or all pairs of runs (across-run ΔtSNR) of the same protocol, and across all subjects to quantify trial variability.

		FLEET *R*=2	FLEET *R*=3	FLEET *R*=4	ss-EPI *R*=2	ms-EPI *R*=2	ms-EPI *R*=3	ms-EPI *R*=4
7T	**normalized tSNR**	1.12±0.09	1.07±0.06	0.92±0.05	0.94±0.05	0.83±0.10	0.77±0.07	0.76±0.08
	normalized tSNR % variation	7.9%	5.6%	6.0%	5.1%	12.5%	9.0%	10.7%
	FWHM of within-run ΔtSNR	0.12±0.04	0.12±0.03	0.11±0.01	0.11±0.02	0.10±0.02	0.11±0.02	0.10±0.01
	FWHM of across-run ΔtSNR	0.12±0.04	0.11±0.03	0.10±0.03	0.12±0.04	0.24±0.09	0.23±0.08	0.15±0.04
	median of across-run ΔtSNR	0.02±0.06	0.00±0.03	0.00±0.03	−0.01±0.03	−0.02±0.07	−0.01±0.06	0.00±0.06
3T	**normalized tSNR**	1.07±0.03	0.97±0.03	0.79±0.02	0.98±0.02	0.95±0.04	0.86±0.03	0.73±0.02
	normalized tSNR % variation	3.1%	3.5%	2.8%	2.1%	4.3%	4.0%	3.0%
	FWHM of across-run ΔtSNR	0.07±0.01	0.07±0.01	0.06±0.00	0.06±0.00	0.12±0.04	0.09±0.02	0.07±0.01

Table 2

Summary of results from a Wilcoxon rank-sum test used to compare FWHM of across-run ΔtSNR between different acquisitions acquired at 3T and 7T. Bolded entries correspond to the main comparisons of interest, i.e., between ms-EPI ACS and FLEET ACS with matching acceleration factor, significant differences are marked in red.

across-run ΔtSNR (FWHM)						
7T	**FLEET *R*=2**	**FLEET *R*=3**	**FLEET *R*=4**	**ss-EPI *R*=2**	**ms-EPI *R*=2**	**ms-EPI *R*=3**
FLEET *R*=3	0.08					
FLEET *R*=4	<0.05	0.31				
ss-EPI *R*=2	0.71	0.08	<0.05			
ms-EPI *R*=2	**<0.01**	<0.01	<0.01	<0.01		
ms-EPI *R*=3	<0.01	**<0.01**	<0.01	<0.01	0.80	
ms-EPI *R*=4	<0.05	<0.01	**<0.01**	<0.05	<0.05	<0.05
3T	**FLEET *R*=2**	**FLEET *R*=3**	**FLEET *R*=4**	**ss-EPI *R*=2**	**ms-EPI *R*=2**	**ms-EPI *R*=3**
FLEET *R*=3	0.20					
FLEET *R*=4	<0.01	<0.05				
ss-EPI *R*=2	0.06	0.96	<0.01			
ms-EPI *R*=2	**<0.01**	<0.01	<0.01	<0.01		
ms-EPI *R*=3	<0.01	**<0.01**	<0.01	<0.01	<0.05	
ms-EPI *R*=4	<0.05	<0.05	**<0.01**	<0.01	<0.01	<0.01

Table 3

Summary of the cluster-based measures used to compare across-run tSNR variation between different protocols for data acquired at 7T: Dice coefficient and inter-cluster distance of the spatial clusters of high tSNR values; reported mean and standard deviation (±) values were calculated across all runs of the same protocol, and across all subjects to quantify trial variability.

	FLEET *R*=2	FLEET *R*=3	FLEET *R*=4	ss-EPI *R*=2	ms-EPI *R*=2	ms-EPI *R*=3	ms-EPI *R*=4
Dice coefficient	0.53±0.06	0.57±0.06	0.57±0.09	0.54±0.08	0.37±0.06	0.38±0.06	0.46±0.08
inter-cluster distance [mm]	3.8±0.9	3.5±0.9	3.7±1.2	3.9±1.5	8.2±1.9	8.0±1.6	5.7±1.5